

PAPER • OPEN ACCESS

## Absolute delay calibration by analytical fitting of attosecond streaking measurements

To cite this article: G Inzani *et al* 2024 *J. Phys. Photonics* **6** 025007

View the [article online](#) for updates and enhancements.

You may also like




- [Absolute Potentials of the Standard Hydrogen Electrode \(4.20 V\), Standard Reference Electrodes & Aqueous Redox Couples of Elements](#)  
Raji Heyrovska
- [Absolute photoabsorption cross sections of Sr I from the 5s ionization threshold to the 5p threshold](#)  
C C Chu, H S Fung, H H Wu et al.
- [On absolute instability of free jets](#)  
V Vedeneev and J Zayko



## PAPER

## OPEN ACCESS

## Absolute delay calibration by analytical fitting of attosecond streaking measurements

RECEIVED  
27 September 2023REVISED  
12 January 2024ACCEPTED FOR PUBLICATION  
1 February 2024PUBLISHED  
14 March 2024G Inzani<sup>1,3,\*</sup> , N Di Palo<sup>1</sup> , G L Dolso<sup>1</sup> , M Nisoli<sup>1,2</sup>  and M Lucchini<sup>1,2</sup> <sup>1</sup> Department of Physics, Politecnico di Milano, 20133 Milano, Italy<sup>2</sup> Institute for Photonics and Nanotechnologies, IFN-CNR, 20133 Milano, Italy<sup>3</sup> Present address: Department of Physics, University of Regensburg, 93053 Regensburg, Germany.

\* Author to whom any correspondence should be addressed.

E-mail: [giacomo.inzani@polimi.it](mailto:giacomo.inzani@polimi.it)

Keywords: attosecond science, light–matter interaction, strong-field physics

Original Content from  
this work may be used  
under the terms of the  
[Creative Commons  
Attribution 4.0 licence](https://creativecommons.org/licenses/by/4.0/).Any further distribution  
of this work must  
maintain attribution to  
the author(s) and the title  
of the work, journal  
citation and DOI.

## Abstract

An accurate temporal characterization of both pump and probe pulses is essential for the correct interpretation of any pump-probe experiment. This is particularly true for attosecond spectroscopy, where the pulses are too short to be directly measured with electronic devices. However, when measuring the absolute timing between a light waveform and the related photoinduced physical phenomenon, such characterization does not suffice. Here, we introduce a new method called rACE (refined Analytical Chirp Evaluation), which retrieves both pump and probe pulses while establishing a direct relation between the reconstructed time axis and the experimental delay. This feature is particularly relevant for the extraction of absolute time delays, a growing field in attosecond spectroscopy. In this work, we prove the robustness of rACE with simulated datasets involving the effect of pulse chirp, distinctive target attributes, and non-isolated attosecond pulses, which normally constitute challenging situations for standard methods. For all the cases reported here, rACE achieves a precise absolute delay calibration with an accuracy better than the atomic unit of time. Its successful application to attosecond experimental measurements makes it a fundamental tool for attaining sub-cycle absolute temporal resolution, enabling new investigations of lightwave-driven ultrafast phenomena.

## 1. Introduction

In the last two decades, developments in laser science and technology fostered the flourishing of a novel field of physics—attosecond science—devoted to the investigation of ultrafast phenomena unfolding on the few-to sub-femtosecond (fs) time scale [1]. Various experimental techniques, either all-optical [2] or based on the detection of photoemitted charged particles or fragments, led to discoveries about ultrafast dynamics in atoms, molecules, and solids, triggered by the interaction with ultrashort light pulses, typically in the infrared (IR) domain [1, 2]. Attoscience also enabled a direct detection of the electric field of light transients [3], allowing to clock light-induced physical phenomena with absolute precision [4–6]. For instance, this unprecedented capability highlighted the role of final-state effects [7] and the related formation of Bloch wave packets [8] during photoemission from solids, and it enabled the unveiling of the intertwined atomic- and bulk-like nature of core excitons [9]. In all these cases, comparing absolute time delays with theory represented the key to unequivocally address the physics at play. While in most of pump-probe experiments, a precise temporal characterization of the employed pulses is sufficient for their correct interpretation, when measuring absolute delays it might not be enough. A novel approach to precisely calibrate the experimental delay axis is thus required.

Since the attosecond (as) radiation is typically in the extreme-ultraviolet (XUV) spectral range, pulse characterization is usually achieved through an XUV-IR two-color photoemission experiment. Depending on the temporal structure of the XUV radiation, this measurement is either called Reconstruction of Attosecond Beating By Interference of Two-photon Transitions (RABBITT) or attosecond streaking [1].

Several approaches were devised to extract the pump and probe temporal profiles from such experiments [10]. In principle, even though in these measurements the origin of the retrieved pump and probe time axes is arbitrary, these quantities should be related. However, most of the reconstruction methods arbitrarily shift one with respect to the other. Although not preventing a proper pulse retrieval, this completely thwarts the determination of absolute time delays.

For photoemission experiments, a possible workaround consists of exploiting a well-characterized target as a reference signal [5, 7]. This reference feature clocks any other phenomenon and, if properly calibrated, allows extracting absolute delays between different processes. A similar approach was devised for all-optical techniques: performing a separated streaking experiment simultaneously with the main measurement, an absolute calibration of the delay axis is possible [6, 9, 11]. However, once a suitable origin of the reconstruction time axis is chosen, this requires to directly relate the pump waveform time axis with the measurement delay axis. Stating such a relationship is not trivial. So far, the most used approach consisted in analyzing the center of mass (CoM) of the streaking trace [11]. In first approximation, this quantity is proportional to the pump vector potential with changed sign [3], but a systematic investigation of the accuracy of this approach is still missing.

Here we show the CoM analysis to be not always correct and introduce rACE (refined Analytical Chirp Evaluation), a new nonlinear fitting routine for streaking spectrograms. Unlike conventional techniques, this approach simultaneously retrieves the XUV intensity profile and IR vector potential while accurately aligning them with the experimental delay axis. Through extensive simulations and reconstructions, we prove its effectiveness and precision, addressing the limitations of existing methodologies. On simulated measurements, rACE achieves an accuracy better than the atomic unit of time (24 as) for the calibration of the absolute delay axis, outperforming conventional methods. We also applied it to two challenging experimental traces, where common approaches fail. Accessing absolute timings in pump-probe experiments is fundamental for exploiting the extreme temporal resolution of attosecond science, and enables the investigation of lightwave-driven phenomena [12] and the ultrafast interplay of charge, spin, and lattice degree of freedom [13] from which many exotic properties of matter originate.

## 2. Limits of the existing approaches

The collection of photoelectron spectra obtained by ionizing a gas target with XUV photons while scanning the relative delay with an intense, few-fs IR pulse, is called spectrogram. Within the strong-field approximation (SFA) [14], it can be described by the following relation (hereafter atomic units are adopted, unless otherwise specified) [15]:

$$S(\mathbf{p}, \tau) = \left| \int_{-\infty}^{+\infty} dt \mathbf{E}_X(t - \tau) \mathbf{d}[\mathbf{p} + \mathbf{A}_{\text{IR}}(t)] e^{-i \int_t^{+\infty} dt' \frac{1}{2} [\mathbf{p} + \mathbf{A}_{\text{IR}}(t')]^2} e^{i I_p t} \right|^2 \quad (1)$$

where  $\mathbf{E}_X(t)$  and  $\mathbf{A}_{\text{IR}}(t)$  are, respectively, the XUV electric field and the IR vector potential,  $\mathbf{p}$  is the photoelectron momentum,  $\tau$  the XUV-IR delay,  $\mathbf{d}(\mathbf{p})$  the transition dipole moment from the atomic ground state to a free electron state and  $I_p$  the ionization potential of the gas target. Away from atomic resonances, if the atomic dipole moment is almost constant in the energy range of interest, the above equation reveals that the IR pulse acts as a phase modulator, streaking the photoelectron spectrum in energy [16]. Since equation (1) depends on both the XUV and IR pulses, reconstruction methods to access their temporal profiles from a spectrogram can be envisioned. However, traditional acquisition systems only measure the intensity of the photoelectron wavepacket, losing their phase. Thus, several iterative approaches were developed to retrieve the phase information and fully characterize the XUV intensity profile as well as the IR field.

### 2.1. FROG CRAB

The most known reconstruction technique is called Frequency-Resolved Optical Gating for Complete Reconstruction of Attosecond Bursts (FROG CRAB) [17]. In brief, it recasts equation (1) in a form suitable for iterative algorithms commonly employed to characterize ultrashort pulses by the Frequency-Resolved Optical Gating (FROG) approach [18]. If both IR and XUV pulses are linearly polarized and the dipole is constant in energy, the spectra of the photoelectrons emitted along the polarization direction can be written as:

$$S(p, \tau) = \left| \int_{-\infty}^{+\infty} dt E_X(t - \tau) d[p] e^{i\phi(t)} e^{i\left(\frac{p^2}{2} + I_p\right)t} \right|^2 \quad (2)$$

where  $p$  is the final electron momentum in the continuum and  $\phi(t)$  is the Volkov phase:

$$\phi(t) \simeq - \int_t^{+\infty} dt' \left[ p_c A_{IR}(t') + \frac{A_{IR}^2(t')}{2} \right] \quad (3)$$

which accounts for the phase accumulated by the wavepacket in the continuum while interacting with the IR field. In equation (3), we replaced the final electron momentum,  $p$ , with the central momentum,  $p_c$ , of the photoelectron wavepacket, performing the so-called central momentum approximation (CMA). This approximation is crucial for the FROG CRAB approach, but can be removed with more refined techniques [19]. By defining a gate,  $G(t)$ , and time-shifted pulse,  $P(t - \tau)$ , function as:

$$G(t) = e^{i\phi(t)}, \quad P(t - \tau) = E_X(t - \tau) d[p], \quad (4)$$

we can rewrite equation (2) as the squared modulus of the Fourier transform of their product:

$$S(p, \tau) = \left| \int_{-\infty}^{+\infty} dt G(t) P(t - \tau) e^{i\omega t} \right|^2 \quad (5)$$

where  $\omega = p^2/2 + I_p$  is the angular frequency. This expression is in the form of a generic blind FROG spectrogram, which can be reconstructed with multiple iterative algorithms (e.g. PCGPA, LSGPA, ePIE, STRIPE) that have been devised on this analogy [20–25].

Over time, these methods became standard tools for characterizing attosecond pulses [10], at least when the XUV bandwidth is not exceedingly broad [26] and when experimental non-idealities can be neglected [27, 28]. Nonetheless, they suffer from a major drawback: the absence of a direct link between the retrieved probe and gate pulse temporal axes and the experimental delay one. This limitation thwarts the achievement of the absolute delay calibration necessary for attosecond-resolved experiments.

Mathematically, equation (5) can be interpreted as the squared modulus of the Fourier transform (indicated as  $\mathcal{F}\{\cdot\}$ ) of the product between the gate and time-shifted pulse functions:

$$S(p, \tau) = |\mathcal{F}\{G(t) P(t - \tau)\}|^2. \quad (6)$$

By exploiting the time-shifting property of the Fourier transform:

$$\mathcal{F}\{x(t - T)\} = e^{-i\omega T} \mathcal{F}\{x(t)\} \quad (7)$$

it is trivial to show that an arbitrary shift along the time axis of both the pulse and gate functions will produce the same spectrogram:

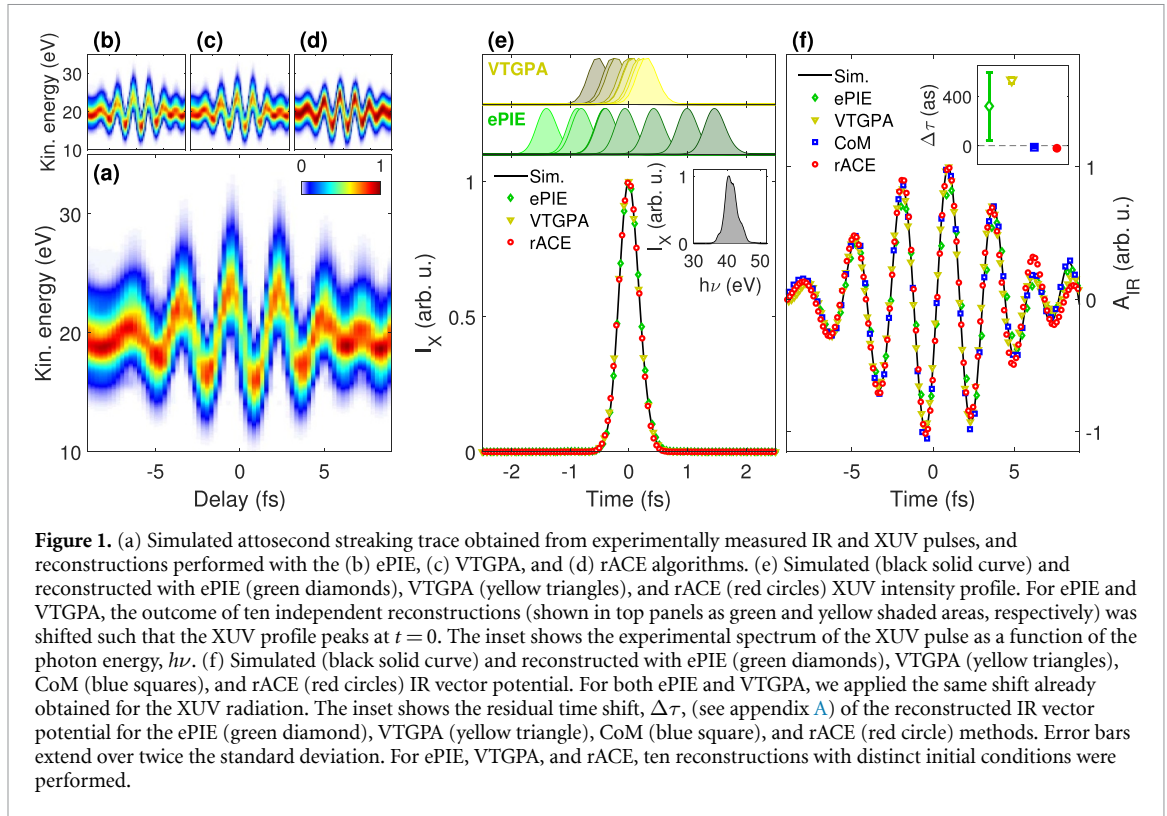
$$|\mathcal{F}\{G(t - T) P(t - T - \tau)\}|^2 = |\mathcal{F}\{G(t) P(t - \tau)\}|^2, \quad (8)$$

inhibiting the direct alignment of the retrieved pulses to the experimental delay axis.

In any pump-probe experiments, therefore, only the relative time delay between the pump and probe pulses,  $\tau$ , is relevant. A proper reconstruction technique should not only provide the correct temporal profile of the pump and probe pulses, but also their exact relative delay. For example, if a spectrogram is simulated with both XUV and IR pulses centered at  $t = 0$  (as in figure 1), a precise reconstruction should give two pulses whose envelopes peak at the same time instant  $T$ . Whatever its value is,  $T$  can be taken as the new zero of the time axis, allowing a direct comparison between the outcome of a pump-probe measurement and the electric field of the pump radiation characterized by an attosecond streaking experiment. However, most of the commonly available methods retrieve a gate pulse,  $G(t + \Delta\tau)$ , with an additional, arbitrary time shift with respect to  $P(t)$ . In the following, we characterize this residual time shift,  $\Delta\tau$ , which prevents a proper alignment of the gate and probe pulses.

To demonstrate the limitations of FROG CRAB-based approaches, we employed equation (1) to simulate an attosecond streaking measurement (figure 1(a)). The input IR field (figure 1(f)) was obtained by a second-harmonic (SH) FROG measurement of pulses emitted by a Ti:Sapphire laser and broadened by an hollow-core capillary compressor, while the spectrum of the XUV radiation (inset in figure 1(e)) generated by high-order harmonic generation (HHG) in argon was measured with an XUV spectrometer [29]. We assumed a group-delay dispersion (GDD) of  $D_{2,X} = 0.01 \text{ fs}^2$  for the XUV radiation.

Figure 1(b) shows one streaking trace reconstructed by exploiting the FROG CRAB approach in tandem with the extended Ptychographic Iterative Engine (ePIE) [22]. Although the reconstructed spectrogram nicely reproduces the simulation, the retrieved XUV intensity profile (green shaded areas in figure 1(e)) does not match the simulated one (figure 1(e), black solid curve). Starting from ten random initial conditions, the



reconstructed XUV intensity is always shifted by a different quantity along the time axis (top panel in figure 1(e)). Assuming as a reference the peak value of the reconstructed XUV intensity profile, we can try to compensate for this shift (figure 1(e), green diamonds). However, if we compare the simulated (black solid curve) and ePIE reconstructed (green diamonds) IR vector potential in figure 1(f), we obtain that the reconstruction has a residual time shift,  $\Delta\tau$ , of  $320 \pm 280$  as (see appendix A for details on its calculation). FROG CRAB-based approaches, therefore, do not allow to temporally relate the reconstructed IR and XUV pulses with the experimentally measured delay axis.

## 2.2. Volkov transform generalized projection algorithm

An alternative technique, which does not rely on the FROG CRAB formalism, is the Volkov transform generalized projection algorithm (VTGPA) [19]. Starting from a scalar version of the SFA equation (1), this method transforms integrals into discrete summations, evaluating the spectrogram over a discrete set of delay and photoelectron energy pairs and performing an error minimization routine. From a mathematical standpoint, this converts the Fourier transform of the FROG CRAB formalism into a discrete transform where the basis is represented by Volkov waves [19]. Moreover, this method does not rely on the CMA.

Figure 1(c) displays the outcome of a VTGPA reconstruction of the simulated streaking trace (figure 1(a)). As for ePIE, despite the good agreement between simulation and reconstructed spectrograms, the retrieved XUV intensity profile from ten independent reconstructions with different initial conditions (yellow shaded areas in figure 1(e)) does not match the simulation input. Also in this case, we can compensate this time shift by assuming the peak value of the XUV intensity as a reference. The obtained profile matches the simulated one (yellow triangles in figure 1(e)). However, if we apply the same time shift to the retrieved IR vector potential in figure 1(f), we obtain a residual delay,  $\Delta\tau$ , of  $532 \pm 25$  as with respect to the simulation. Therefore, also VTGPA does not generally allow an accurate reconstruction of the relative timing between the retrieved XUV and IR pulses.

## 2.3. Center-of-mass method

In an attosecond streaking measurement, the change in central kinetic energy,  $\Delta K$ , of the photoelectron wavepacket is proportional to the IR vector potential at the time instant of ionization,  $\tau$ , with changed sign [3]:

$$\Delta K(\tau) \propto -A_{\text{IR}}(\tau). \quad (9)$$

Therefore, by computing the delay-dependent CoM of the spectrogram,  $S(K, \tau)$ , as a function of the kinetic energy,  $K$ , we can extract the temporal profile of the IR vector potential:

$$A_{\text{IR}}(\tau) \simeq - \frac{\int_0^{+\infty} dK K \cdot S(K, \tau)}{\int_0^{+\infty} dK S(K, \tau)} \quad (10)$$

linking the time and delay axes. This method has been already applied for interpreting attosecond experiments [11, 30–32], and can be further refined by considering an amplitude factor and a target-dependent time shift [33].

Blue squares in figure 1(f) mark the IR vector potential retrieved with the CoM method for the streaking trace represented in figure 1(a). For the considered case, this approach accurately retrieves the IR vector potential with a negligible temporal shift (inset in figure 1(f)) of  $12 \pm 4$  as. However, in section 4 we will show that it fails when applied in more realistic conditions, especially when satellite XUV pulses are present. Therefore, an innovative reconstruction method is imperative to bridge the gap between reconstruction and experimental delay axis for attosecond temporal resolution; this method is rACE.

### 3. Model and algorithm

Starting from equation (2), if the XUV pulse is much shorter than the IR one, the time-dependent Volkov phase can be approximated as constant and equal to its value at the instant of ionization. We can then assume a Gaussian temporal profile for the photoelectron wavepacket,  $\chi_s(t, \tau)$ , generated by the XUV radiation and dressed by the IR pulse, which can be written as [34]:

$$\chi_s(t, \tau) = A_x e^{-\frac{1}{2} \left(\frac{t}{\sigma_x}\right)^2} e^{i[K_s(\tau)t + \frac{1}{2}\beta_s(\tau)t^2]} \quad (11)$$

where  $A_x$  and  $\sigma_x$  are the amplitude and duration of the XUV pulse. The dressing IR pulse changes the central energy,  $K_s$ , and chirp rate,  $\beta_s$ , of the ‘streaked’ photoelectron wavepacket [34]:

$$K_s(\tau) = K_c - p_c A_{\text{IR}}(\tau) + \frac{1}{2} A_{\text{IR}}^2(\tau), \quad \beta_s(\tau) = \beta_x + p_c E_{\text{IR}}(\tau) \quad (12)$$

where  $K_c = p_c^2/2$  and  $p_c$  are, respectively, the central energy and momentum of the wavepacket,  $\beta_x$  is the chirp rate of the XUV pulse and  $E_{\text{IR}} = -\partial A_{\text{IR}}/\partial t$  is the IR electric field. Gagnon and Yakovlev [34] exploited equation (12) to analytically express the bandwidth of the streaked photoelectron wavepacket. This quantity was used for directly extracting the attosecond chirp of the XUV radiation from spectrograms, and the proposed method dubbed Analytical Chirp Evaluation (ACE). In this technique, the IR vector potential was evaluated as the first moments of the streaked photoelectron spectra, i.e. the center of mass of the streaking trace, and the absolute delay calibration was not discussed. Here, we go significantly beyond this approach, obtaining a versatile analytical expression for streaking measurements which allows to access absolute timings in pump-probe experiments.

The spectrogram, in fact, is the squared modulus of the Fourier transform of the time-dependent streaked photoelectron wavepacket of equation (11):

$$S(p, \tau) = |\mathcal{F}\{\chi_s(t, \tau)\}|^2 = |\tilde{\chi}_s(p, \tau)|^2 \quad (13)$$

which can be analytically computed as:

$$\tilde{\chi}_s(p, \tau) = \frac{A_x \sigma_x}{\sqrt{1 - i\beta_s(\tau) \sigma_x^2}} e^{-\frac{[p^2/2 - K_s(\tau)]^2 \sigma_x^2}{2[1 - i\beta_s(\tau) \sigma_x^2]}}. \quad (14)$$

Assuming an analytical expression for the IR field of the form:

$$A_{\text{IR}}(t) = A_0 \mathcal{E}(t) \cos \left[ \omega_{\text{IR}}(t - t_0) + \frac{1}{2} \beta_r (t - t_0)^2 + \phi_{\text{CEO}} \right] \quad (15)$$

where  $t_0$  is an arbitrary time shift,  $A_0$  the amplitude term,  $\omega_{\text{IR}}$  the angular frequency of the IR radiation,  $\beta_r$  the associated chirp rate,  $\phi_{\text{CEO}}$  the IR carrier-envelope offset, and  $\mathcal{E}(t)$  the Gaussian envelope:

$$\mathcal{E}(t) = e^{-\frac{(t-t_0)^2}{2\sigma_{\text{IR}}^2}}, \quad (16)$$



we obtain analytical expressions for  $K_s$  and  $\beta_s$  in equation (12), which inserted in equation (14) give an analytical function describing the experimental spectrogram. We implemented this expression in a nonlinear least-squares curve fitting tool (a Matlab built-in function), which allows retrieving parameters for the XUV and IR pulses by minimizing the distance between the input and reconstructed spectrograms.

A crucial point is that, in equation (11), the Gaussian XUV envelope peaks at  $t = 0$ . Moreover, analytically computing the Fourier transform in equation (14) is equivalent to setting  $T = 0$  in equation (8) for FROG CRAB methods; this is not the case for ePIE and VTGPA, as each reconstruction is shifted by a different arbitrary time value (figure 1(e)). These characteristics are essential for achieving the desired absolute delay calibration and relate the reconstruction time axes to each other and with the experimental delay one, once a suitable reference time zero (in our case, that corresponding to the peak intensity of the XUV profile) is chosen.

Figure 1(d) shows the rACE reconstruction of the streaking trace represented in figure 1(a). Despite the analytical expressions for both the XUV and IR pulses only allow reconstructing Gaussian pulses, in figures 1(e)–(f) deviations from the simulated XUV and IR profiles—which, being experimentally measured, are not perfect Gaussians—are negligible. We stress that the rACE approach can be generalized, at a similar computational cost, for any analytical definition of the IR and XUV profiles such that (i) both  $A_{\text{IR}}$ , its derivative, its integral, and the integral of  $A_{\text{IR}}^2$  are analytical expressions, and (ii) the Fourier transform of the temporal profile of the photoelectron wavepacket is an analytical expression. Any functional form which satisfies these requirements and well approximates the IR and XUV pulses is suitable for rACE. A more flexible parametrization of the IR pulse, for instance as the one implemented in VTGPA [19], could further generalize the rACE approach allowing an arbitrary IR envelope. However, it would require additional computational resources, without substantially improving the retrieval of the absolute delay (see section 4.4).

In this specific case, rACE accurately retrieves the timing of the IR vector potential within  $20 \pm 7$  as (inset of figure 1(f)). It outperforms FROG CRAB-based methods by an order of magnitude and obtains a result comparable with the CoM method, thus allowing for a precise absolute calibration of the delay axis. Since, even in this simple case, ePIE and VTGPA perform worse than the CoM approach, from hereon we will only use the latter as a benchmark.

## 4. Robustness on the experimental parameters

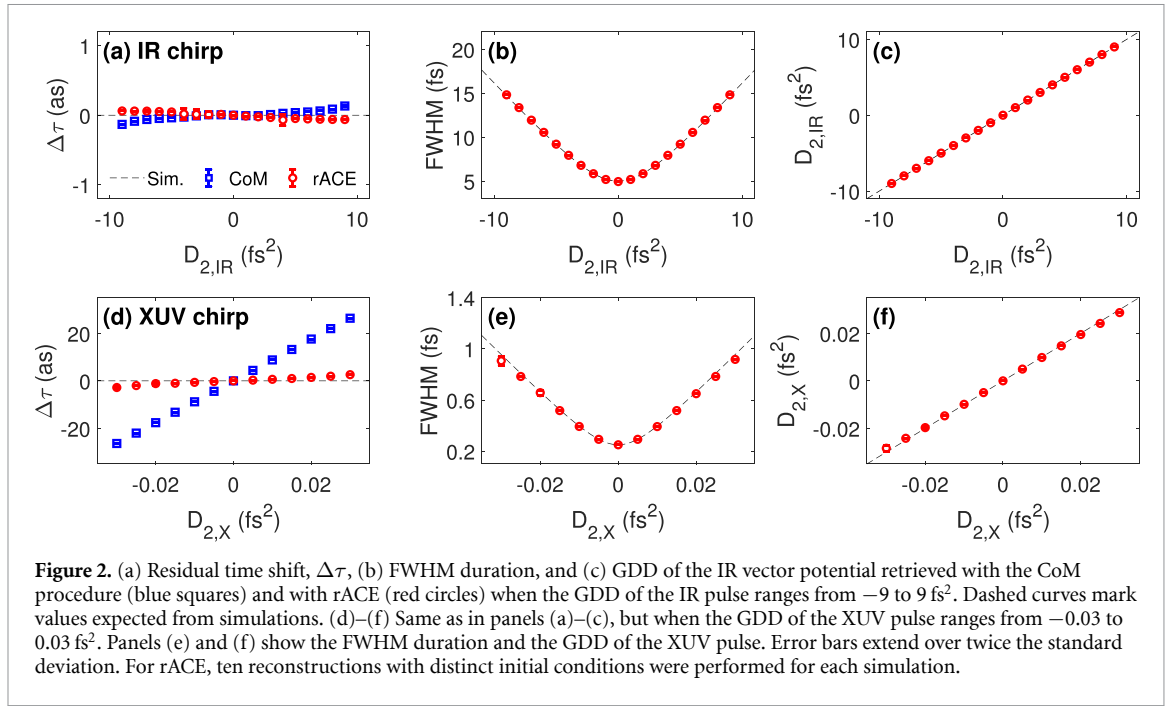
A crucial characteristic of pulse reconstruction methods is their robustness on experimental parameters. Besides the known shortcomings of attosecond streaking measurements [27] and SFA-based descriptions [28, 33, 35], the accuracy of simplified approaches can be further hindered by their approximations. In this section, we delve into more complex scenarios to highlight potential limitations, showing that rACE surpasses the CoM approach and allows a precise absolute calibration with attosecond temporal resolution. In all simulations here reported, we assumed the interaction of a radially uniform two-color laser field with a single atomic target, neglecting any ensemble or volume effects. Previous works demonstrated that volume effects can alter the retrieved IR intensity and XUV pulse duration in extreme experimental conditions, without hindering access to spectroscopic information as the photoionization time delays [28, 35]. Unless otherwise specified, the IR pulses have a transform-limited Gaussian intensity profile with full-width at half-maximum (FWHM) duration of 5 fs, central wavelength of 800 nm, and peak intensity of  $2 \times 10^{12}$  W cm<sup>-2</sup> in vacuum, while the XUV pulses have a transform-limited Gaussian intensity profile with FWHM duration of 250 as, central photon energy of  $25 \hbar\omega_{\text{IR}} \simeq 38.75$  eV and peak field amplitude of  $1 \times 10^9$  V cm<sup>-1</sup>. We always assumed neon as a gas target ( $I_p \simeq 21.56$  eV).

### 4.1. Chirp of the IR and XUV pulses

Exploring the impact of the chirp of the IR and XUV radiation on the timing of the reconstructed vector potential, we performed simulations based on equation (1) varying the GDD,  $D_2$ . For the IR radiation, the GDD was changed between  $-9$  and  $9$  fs<sup>2</sup> in figures 2(a)–(c), while for the XUV pulses in figures 2(d)–(f), it ranged from  $-0.03$  to  $0.03$  fs<sup>2</sup>. For the IR chirp, both rACE and the CoM procedure produce extremely accurate results (figure 2(a)). Instead, considering the XUV chirp, the CoM approach displays shifts in the retrieved IR vector potential up to 26 as, while rACE consistently yielded phase delays below 3 as (figure 2(d)). Furthermore, rACE accurately characterizes the FWHM duration (figures 2(b), (e)) and GDD (figures 2(c), (f)) of both pulses, while the properties of the XUV pulse are inaccessible by the CoM method.

### 4.2. Photoionization cross-section and phase

A common assumption of pulse retrieval algorithms is the wavepacket approximation [36–38]. From equation (1), the dependence of the dipole moment of the XUV-induced transitions on the IR vector



potential is typically neglected ( $d[\mathbf{p} + \mathbf{A}_{\text{IR}}(t)] \simeq d[\mathbf{p}]$ ) and its product with the Fourier transform of the XUV electric field,  $\tilde{E}_X$ , gives the photoelectron wavepacket:

$$\tilde{\chi}(\mathbf{p}) = \tilde{E}_X(\mathbf{p}) d[\mathbf{p}]. \quad (17)$$

In most of the pulse retrieval algorithms, the reconstructed quantity is not the XUV electric field, but its product with the transition dipole moment, i.e. the photoelectron wavepacket. A customary choice is then to assume  $d(\mathbf{p})$  constant and thus  $\tilde{\chi} \simeq \tilde{E}_X$ . This assumption is experimentally justified by carefully choosing the gas target to avoid any significant distortion of the photoelectron wavepacket [36], but the spectral filter operated by  $d(p)$  can lead to systematic errors in the delay axis calibration.

Under the assumptions of equation (2), we can write the dipole moment in the frequency domain as the product of its modulus, also called atomic cross-section,  $\sigma_{\text{at}}(p)$ , and a phase term,  $\eta(p)$ , called atomic phase:

$$d(p) = |d(p)| e^{i\eta(p)} = \sigma_{\text{at}}(p) e^{i\eta(p)}. \quad (18)$$

For noble gases, the experimental values for the atomic cross-section [39] and calculated atomic phases [40] can be found in the literature (see figure 3(c) for the case of Ne and Ar). Therefore, we can exploit them to account for the atomic dipole of the gas target in the rACE algorithm.

Figure 3(a) shows the residual time shift,  $\Delta\tau$ , of the reconstructed IR vector potential for the CoM procedure (blue square) and for rACE neglecting (orange triangle) or including (red circle) the atomic cross-section. Since far from resonances its only effect is a minor distortion of the spectral intensity of the wavepacket, all methods produce very accurate results.

For the atomic phase, instead, we can expand it in a Taylor series around the central momentum,  $p_c$ , of the wavepacket. The constant term will give a phase offset which vanishes in the squared modulus of equation (13). From the definition of group delay:

$$\tau_{\text{at}}(E_c) = \left. \frac{\partial \eta}{\partial E} \right|_{E=E_c} = \left. \frac{\partial \eta}{\partial K} \right|_{K=K_c} = \left. \frac{1}{p_c} \frac{\partial \eta}{\partial p} \right|_{p=p_c} \quad (19)$$

where  $E = K + I_p$  is the photon energy and  $E_c$  its central value. Therefore, the first-order derivative of the atomic phase gives a linear phase term that will introduce an additional delay,  $\tau_{\text{at}}$ , to be summed to the experimental pump-probe delay,  $\tau$ . The atomic group delay, represented in figure 3(d), can amount up to 100 as. Neglecting it, both in the rACE and CoM procedures, gives a systematic shift of the retrieved IR vector potential of a few tens attoseconds ( $-33$  as in figure 3(b)), while summing it to the experimental delay allows rACE to produce accurate results.

In the Taylor expansion, higher-order terms will give an additional energy-dependent phase to the photoelectron wavepacket. As an example, we can compute the additional GDD associated with the atomic phase, represented in figure 3(e), as:



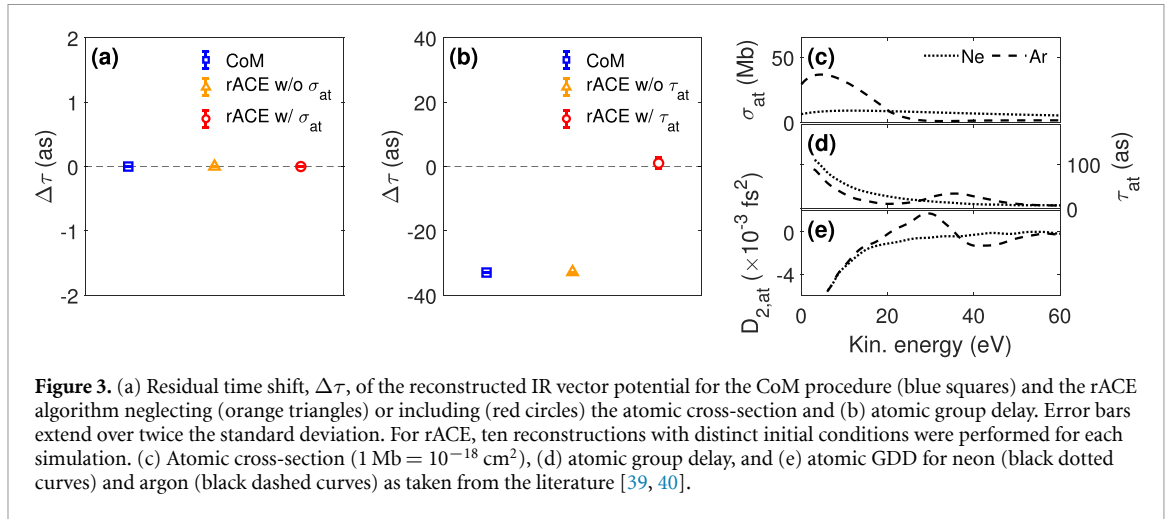


**Figure 3.** (a) Residual time shift,  $\Delta\tau$ , of the reconstructed IR vector potential for the CoM procedure (blue squares) and the rACE algorithm neglecting (orange triangles) or including (red circles) the atomic cross-section and (b) atomic group delay. Error bars extend over twice the standard deviation. For rACE, ten reconstructions with distinct initial conditions were performed for each simulation. (c) Atomic cross-section (1 Mb =  $10^{-18}$  cm<sup>2</sup>), (d) atomic group delay, and (e) atomic GDD for neon (black dotted curves) and argon (black dashed curves) as taken from the literature [39, 40].

$$D_{2,\text{at}}(E_c) = \left. \frac{\partial \tau_{\text{at}}}{\partial E} \right|_{E=E_c} = \frac{1}{p_c^2} \left. \frac{\partial^2 \eta}{\partial p^2} \right|_{p=p_c}. \quad (20)$$

Both for Ne and Ar, the atomic GDD is very small, about one order of magnitude smaller than what considered in figures 2(d)–(f). Thus, its impact on the retrieved IR vector potential is expected to be negligible, supporting our choice of neglecting any atomic phase term apart from the atomic group delay.

Before concluding, we remark that we do not suggest the CoM or rACE approaches to extract energy-dependent photoemission time delays from attosecond streaking spectrograms. First, they may be more sensitive to the actual IR and XUV pulse envelopes than the calibration of the absolute delay discussed in this manuscript. Second, since the meaningful photoemission time delay information is usually extracted by performing a phase-delay difference, any errors in determining the time zero introduced by blind FROG approaches (see section 2.1) will cancel out and not affect the results. rACE, instead, is preferred when a streaking spectrogram, performed in a known calibration target, is used to extract the pump temporal profile, to be compared with the fast oscillating part of a simultaneous pump-probe experiment [6, 9, 11, 41–43].

### 4.3. Satellite XUV pulses

In realistic experimental conditions, generating a perfectly isolated single attosecond pulse can be challenging. Noise and instabilities in the driving laser are strongly enhanced in the HHG process, leading to the emission of satellite pulses. Depending on the adopted gating scheme, pre- and post-pulses can be separated from the main XUV burst by a half-cycle [44, 45] or a full optical cycle [46] of the driving radiation. Satellite pulses generate additional photoelectron wavepackets which interfere with the main one, producing spectral modulations and interference patterns [47]. By reshaping the spectral amplitude, the interference pattern can cause the CoM to deviate from the IR vector potential, hindering a proper extraction.

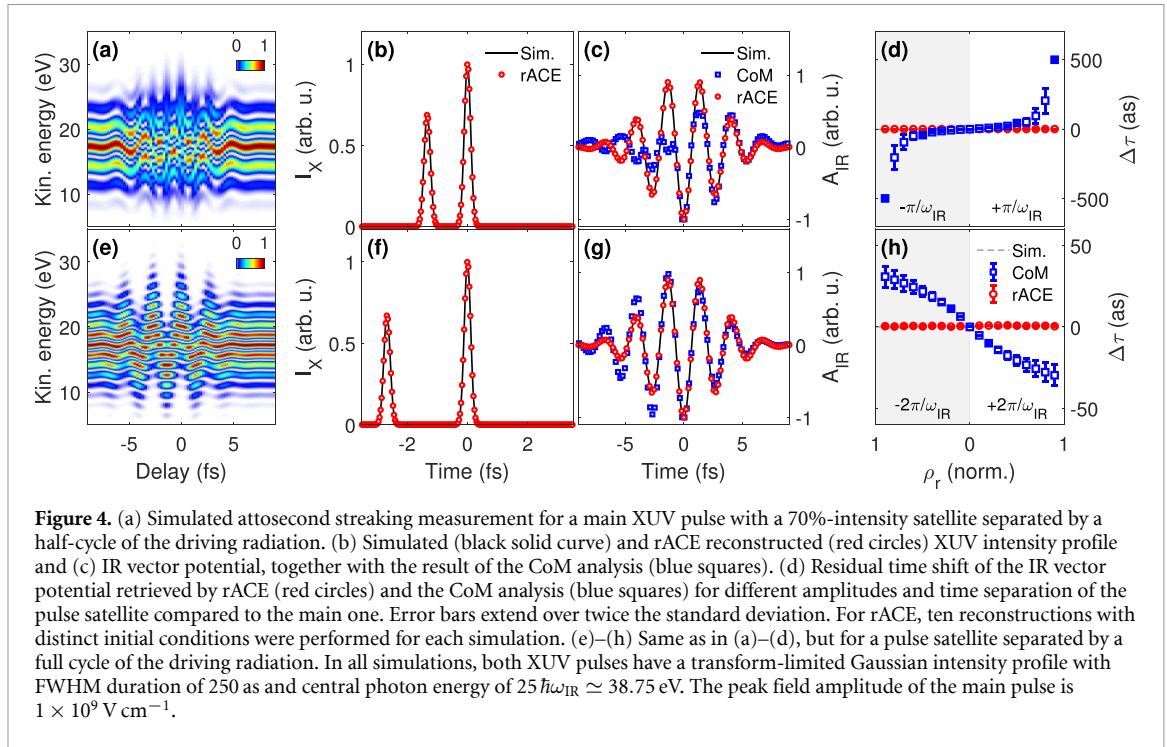
We extended the rACE approach to include a satellite pulse by considering a replica of the main photoelectron wavepacket described in equation (11), but scaled in amplitude by a factor  $\rho_r$  and shifted in time by  $\delta_t$ :

$$\chi(t, \tau) = \chi_s(t, \tau) + \rho_r \chi_s(t - \delta_t, \tau - \delta_t) e^{-i\omega_{\text{IR}}\delta_t}. \quad (21)$$

The additional phase term for the replica accounts for the acceleration of the satellite wavepacket in the opposite (for  $\delta_t = \pm\pi/\omega_{\text{IR}}$ ) or same (for  $\delta_t = \pm 2\pi/\omega_{\text{IR}}$ ) direction with respect to the main one depending on their temporal distance. Fourier transforming equation (21), we obtain the expression for the spectrogram to be used in the fit. This requires calculating of the Volkov phase of the two wavepackets (appendix B); further details on the derivation are reported in appendix C.

Figures 4(a) and (e) show two spectrograms simulated with equation (1) by considering a satellite XUV pulse, 70% in intensity compared to the main one, respectively separated by a half-cycle and a full cycle of the driving radiation. The traces are significantly more structured than those obtained from an isolated single attosecond pulse (figure 1(a)). Despite the increased complexity, rACE accurately retrieves both the XUV intensity profile (figures 4(b), (f)) and the IR vector potential (figures 4(c), (g)). The CoM analysis, in turn, fails in reconstructing the IR vector potential.

Simulations were performed while changing the amplitude of the pulse replicas between 0 and 90% of the main peak intensity, both when the satellite pulse comes before ( $\delta_t < 0$ ) or after ( $\delta_t > 0$ ) the main one.



For a half-cycle separation (figure 4(d)), the absolute residual time shift is up to  $499 \pm 8$  as. Considering instead a full-cycle separation (figure 4(h)), at most it amounts to  $31 \pm 6$  as. In both cases, rACE has a residual time shift smaller than 1 as. It is worth noticing that this effect is clearly stronger when the pulse replica is separated by a half-cycle of the IR radiation: the photoelectron wavepackets generated by the two replicas are accelerated in opposite directions, strongly distorting the IR vector potential retrieved by the CoM. For a full-cycle separation, instead, both wavepackets are accelerated in the same direction; this mainly distorts the IR envelope retrieved by the CoM, with a smaller effect on the phase of the carrier. Notably, the half-cycle separation, where the CoM analysis shows larger residual time shifts, is the standard condition for most of the experimental implementations. The rACE approach, in turn, outperforms it, proving accurate irrespectively of the satellite pulse amplitude.

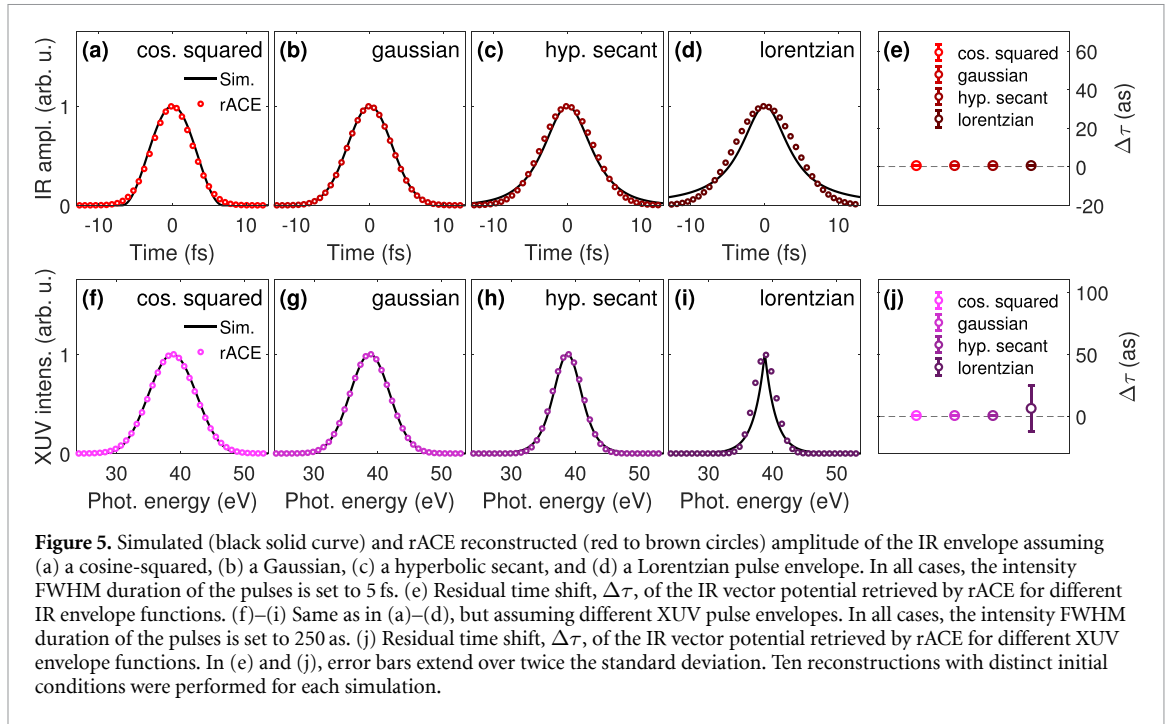
It is worth noticing that a correct mathematical description of the XUV intensity profile is crucial. While a non-Gaussian spectral shape has a minor influence on the accuracy of the absolute delay calibration (see figure 1 and section 4.4), underestimating the number of XUV pulses (e.g. considering only one XUV pulse when a satellite is present) hinders convergence. Although it is not possible to extract reliable information from non-converged results, we expect the residual time shift to be comparable to the CoM one, as this approach implicitly describes a streaking measurement as a single Dirac-like XUV pulse sampling the IR waveform.

As underestimating the number of satellite pulses hinders convergence, two practical strategies to set up the analytical model for rACE are possible. First, a visual inspection of the periodic energy modulation of the photoelectron spectra already hints at the presence of satellite pulses and their time distance from the main one. This allows assuming a reasonable multi-Gaussian model with a large enough number of free parameters. Alternatively, it is possible to reconstruct the attosecond streaking trace with another method [19–25] and use the retrieved XUV profile to determine the number of pulses. We regard both approaches to be equally valid.

#### 4.4. IR and XUV envelopes

In the rACE method, we assumed a Gaussian envelope for both the XUV and IR pulses. In real experiments, however, this could not be the case, and more complicated shapes could arise. We checked the impact of this approximation by reconstructing attosecond streaking measurements simulated with different XUV and IR envelope functions. To keep fixed the FWHM intensity duration of the pulses, we defined a cosine-squared envelope as:

$$\mathcal{E}(t) = \begin{cases} \cos^2\left(\frac{\pi t}{p}\right), & \text{for } -\frac{p}{2} \leq t \leq \frac{p}{2} \text{ and } p = \frac{\pi\sqrt{\ln(2)}\sigma}{\arccos\left(2^{-\frac{1}{4}}\right)} \\ 0, & \text{elsewhere} \end{cases} \quad (22)$$



In the same spirit, we defined a hyperbolic secant envelope:

$$\mathcal{E}(t) = \left( \frac{\ln(1 + \sqrt{2})}{2\sqrt{\ln(2)}\sigma} \right)^{\frac{1}{2}} \operatorname{sech} \left( \frac{2t \ln(1 + \sqrt{2})}{2\sqrt{\ln(2)}\sigma} \right), \quad (23)$$

and a Lorentzian envelope:

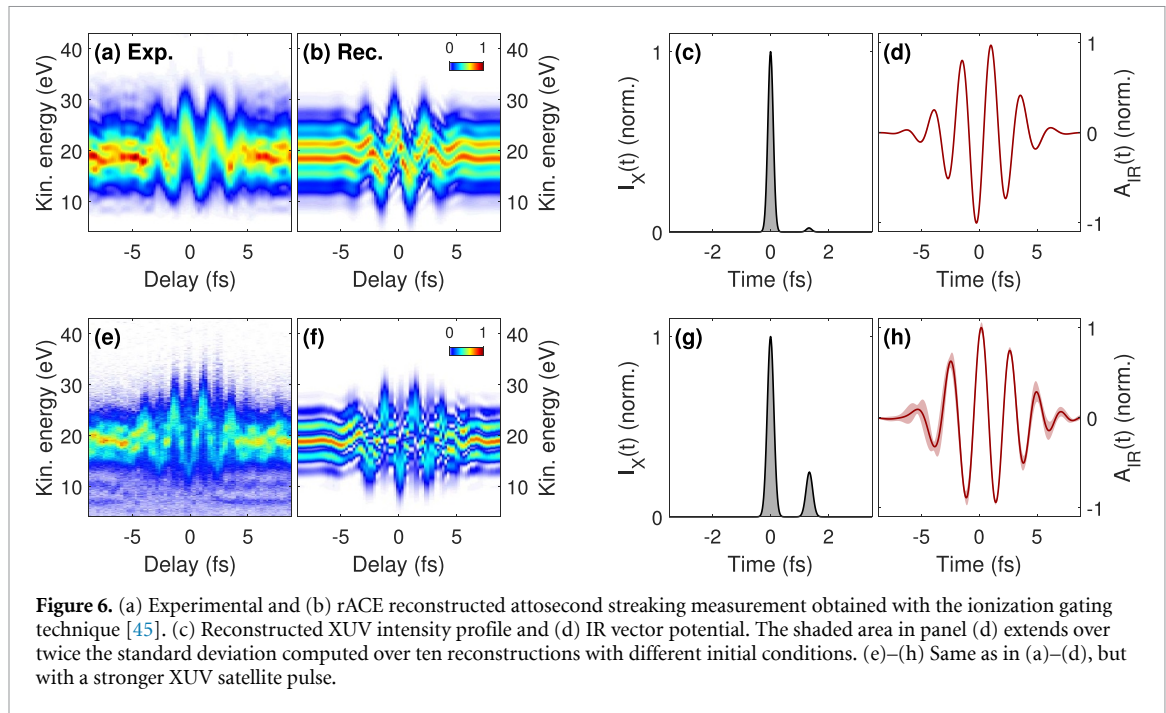
$$\mathcal{E}(t) = \left( \frac{4\sqrt{\sqrt{2}-1}}{\pi\sqrt{\ln(2)}\sigma} \right)^{\frac{1}{2}} \frac{1}{1 + \frac{(\sqrt{2}-1)t^2}{\ln(2)\sigma^2}} \quad (24)$$

where  $\sigma$  is the standard deviation of the associated Gaussian envelope. We performed two sets of simulations and reconstructions. In the first set (figures 5(a)–(e)), we simulated a single Gaussian XUV attosecond pulse and we changed the envelope function of the IR pulse. In the second set (figures 5(f)–(j)), we simulated a Gaussian IR pulse and changed the envelope function of the single XUV attosecond pulse. In all cases, we assumed intensity FWHM durations of 5 fs for the IR and 250 as for the XUV.

In all panels of figure 5, colored markers show the result of the rACE reconstructions, which assume Gaussian pulses. Considering the distinct IR envelopes (figures 5(a)–(d)), rACE converges to the Gaussian shape that best fits the simulated function. Despite the discrepancy between the simulation and the reconstruction being particularly evident for the Lorentzian pulse (figure 5(d)), the residual time shift of the IR vector potential,  $\Delta\tau$ , retrieved by rACE is in all cases below 1 as (figure 5(e)).

The same holds when different XUV pulse envelopes are considered (figures 5(f)–(i)). In this case, the rACE approach fits the XUV spectral intensity with a Gaussian profile. This approximation is particularly good for cosine squared and hyperbolic secant envelopes (figures 5(f), (h)), but it leads to large errors for Lorentzian pulses (figure 5(i)). From figure 5(j), the residual time shift,  $\Delta\tau$ , is below 1 as only for the cosine squared, Gaussian and hyperbolic secant profiles, while Lorentzian pulses leads to a larger shift ( $6 \pm 18$  as).

While the above examples underline the robustness of rACE with pulses characterized by an even temporal envelope, they do not address its applicability to strongly distorted pulses. Although rACE can correctly treat asymmetric IR profiles (see the example in figure 1), the current version may not properly approximate uneven XUV pulses, as their spectral phase is limited to a quadratic term. Nevertheless, since second-order dispersion usually dominates attosecond pulse generation, this discussion covers the majority of realistic experimental scenarios. Therefore, we proved rACE to be reliable for any symmetric XUV and IR envelope functions considered, although strongly distorted or significantly asymmetric XUV spectra can decrease its precision or, in extreme conditions, hinder convergence.



## 5. Reconstruction of experimental measurements

In previous sections, we demonstrated the efficacy of the rACE method in characterizing IR and XUV radiation across diverse scenarios, always obtaining an absolute calibration of the delay axis with a precision below the atomic unit of time. In particular, while for ideal, ‘well-behaved’ spectrograms both rACE and the CoM method give consistent results, only the former is accurate in more realistic and challenging conditions. To finally test its usefulness, we apply it to real measurements. The experimental setup used to obtain them is described elsewhere [29].

Figures 6(a) and (b) show the experimental and reconstructed attosecond streaking trace obtained from a neon jet using the ionization gating technique [45]. An intense IR pulse is tightly focused onto the gas target to achieve a peak intensity exceeding the saturation one. This leads to a complete ionization of the noble gas atoms on the rising edge of the driving pulse, confining the emission of the XUV radiation in just one half-cycle, leading to the generation of a single attosecond pulse. The reconstructed XUV intensity profile (figure 6(c)) is consistent with this picture: it shows an almost isolated single attosecond pulse, with a small pulse replica at a half-cycle of the driving IR radiation, coming from an incomplete ionization of the medium, which modulates the photoelectron spectrum. The reconstructed IR pulse (figure 6(d)), which is a fraction of the radiation driving the HHG process, has a duration compatible with that required by the ionization gating technique [45]. We also accounted for the additional  $\sim 30$ -as atomic group delay associated with the atomic phase of the Ne gas target in the reconstruction. At variance with the CoM analysis, the rACE technique is capable of dealing with all these non-idealities, which could potentially hinder a precise delay calibration.

For longer IR pulses (figure 6(h)), the gas target is only partially ionized within the first half-cycle of the driving radiation, and a satellite XUV pulse is emitted at a half-cycle separation (figure 6(g)). As the photoelectrons generated by the main and satellite XUV pulses experience an IR field with opposite sign, the spectrogram is characterized by an interference pattern (figure 6(e)) which strongly depends on the pulse parameters. However, fluctuations, ensemble effects and noise smear it [28, 47], increasing the complexity of the reconstruction (figure 6(f)). To improve accuracy, constraints on the fit parameters, in particular on the satellite amplitude, are fundamental.

Therefore, also on experimental traces, rACE proves to be a versatile tool, which enables an absolute delay calibration in diverse and challenging experimental conditions.

## 6. Conclusions

In conclusion, we have demonstrated that FROG CRAB-based methods do not allow relating the time axis of the reconstructed XUV and IR pulses with the experimental delay axis of the measured spectrogram. To overcome this limitation, we propose a refined version of the Analytical Chirp Evaluation method, called rACE, to fit attosecond streaking measurements analytically. The derivation of a flexible expression for

spectrograms and its implementation in a nonlinear fitting routine allows retrieving both the XUV intensity profile and the IR vector potential, while keeping a precise relationship between the time and delay axes. This novel possibility enables clocking pump-induced features in any other simultaneous experiment, as they can be directly compared with the vector potential that is inducing them. We tested rACE by reconstructing simulated spectrograms in several challenging conditions, studying its precision against the chirp of the XUV and IR pulses, the target-dependent photoionization cross-section and phase, and the presence of satellite XUV pulses. Comparing the simulated vector potential with the rACE reconstruction, we obtained significantly better results than by extracting it from the CoM of the spectrogram. In all tested conditions, rACE showed superior performances, accurately characterizing the IR waveform with respect to the delay axis with a precision below the time atomic unit. These results are relevant for any simultaneous differential delay experiment in two separate systems, possibly even exploiting distinct (e.g. all-optical) attosecond techniques. The successful application to challenging experimental traces makes it a valuable tool to achieve attosecond temporal resolution in spectroscopic measurements of absolute timings.

### Data availability statement

The data cannot be made publicly available upon publication because they are not available in a format that is sufficiently accessible or reusable by other researchers. The data that support the findings of this study are available upon reasonable request from the authors.

### Acknowledgments

This project has received funding from the European Research Council (ERC) under the European Union's Horizon 2020 research and innovation programme (Grant Agreement No. 848411 title AuDACE) and from MIUR FARE (Grant No. R209LXZRSL, title PHorTUNA).

### Appendix A. Residual time shift of the reconstructed IR vector potential

To quantify the time shift between the simulated,  $A_{\text{Sim}}(t)$ , and reconstructed,  $A_{\text{Rec}}(t)$ , IR vector potential, regardless of the reconstruction method, we computed the phase delay between the two quantities [9]. Since any shift of the reconstructed vector potential along the time axis with respect to the simulated one will result in an additional phase term in the frequency domain, we can define  $\tilde{A}_{\text{Sim}}(\omega)$  and  $\tilde{A}_{\text{Rec}}(\omega)$ , respectively, the associated Fourier-transformed quantities. Then, we compute the product of the latter by the complex conjugate of the former:

$$\tilde{P}(\omega) = \tilde{A}_{\text{Rec}}(\omega) \cdot \tilde{A}_{\text{Sim}}^*(\omega) \quad (\text{A.1})$$

where  $*$  represents the complex conjugate. The squared modulus of the product will peak at the central IR frequency,  $\omega_{\text{IR}}$ , while its phase will give the phase difference between the simulated and the reconstructed IR vector potential. We can extract the phase difference between simulation and reconstruction by a weighted average procedure:

$$\phi = \frac{\int d\omega |\tilde{P}(\omega)|^2 \angle \tilde{P}(\omega)}{\int d\omega |\tilde{P}(\omega)|^2} \quad (\text{A.2})$$

where  $\angle$  indicates the phase and the integration domain extends over frequencies for which  $|\tilde{P}(\omega)|^2$  is larger than 50% of its peak value. The related variance is:

$$\sigma_{\phi}^2 = \frac{\int d\omega |\tilde{P}(\omega)|^2 [\angle \tilde{P}(\omega) - \phi]^2}{\int d\omega |\tilde{P}(\omega)|^2}. \quad (\text{A.3})$$

By dividing these quantities by the central IR frequency,  $\omega_{\text{IR}}$ , we obtain the residual time shift between the simulated and the reconstructed IR vector potential, and the associated variance:

$$\Delta\tau = \frac{\phi}{\omega_{\text{IR}}}, \quad \sigma_{\Delta\tau}^2 = \frac{\sigma_{\phi}^2}{\omega_{\text{IR}}^2}. \quad (\text{A.4})$$

## Appendix B. Analytical expression of the IR field and of the Volkov phase

One of the keys of the rACE approach is the analytical definition of the XUV and IR pulses, which allows deriving an analytical expression for the spectrogram. Considering equation (1), this also means computing the IR electric field and the Volkov phase (equation (3)) analytically.

Starting from the definition of the IR vector potential in equation (15), by deriving this expression we can write the IR electric field as:

$$E_{\text{IR}}(t) = A_0 \mathcal{E}(t) \left\{ [\omega_{\text{IR}} + \beta_r(t-t_0)] \cdot \sin \left[ \omega_{\text{IR}}(t-t_0) + \frac{1}{2}\beta_r(t-t_0)^2 + \phi_{\text{CEO}} \right] + \frac{t-t_0}{\sigma_{\text{IR}}^2} \cdot \cos \left[ \omega_{\text{IR}}(t-t_0) + \frac{1}{2}\beta_r(t-t_0)^2 + \phi_{\text{CEO}} \right] \right\}. \quad (\text{B.1})$$

This expression will give the chirp of the streaked photoelectron wavepacket in equation (12).

Instead, from the definition of Volkov phase in equation (3), we can write it as:

$$\phi(t) = -p_c \int_t^{+\infty} dt' A_{\text{IR}}(t') - \int_t^{+\infty} dt' \frac{A_{\text{IR}}^2(t')}{2} \quad (\text{B.2})$$

and rewriting the cosine term in equation (15) as the sum of two complex exponentials, the first integral gives:

$$\int_t^{+\infty} dt' A_{\text{IR}}(t') = \frac{A_0 \sigma_{\text{IR}} \sqrt{\pi}}{2} \left\{ \frac{(-1)^{\frac{1}{4}} e^{i\phi_{\text{CEO}}} e^{-\frac{i\omega_{\text{IR}}^2 \sigma_{\text{IR}}^2}{2\beta_r \sigma_{\text{IR}}^2 + 2i}}}{\sqrt{2\beta_r \sigma_{\text{IR}}^2 + 2i}} \left[ \text{erf} \left( \frac{(-1)^{\frac{3}{4}} [(t-t_0)(\beta_r \sigma_{\text{IR}}^2 + i) + \omega_{\text{IR}} \sigma_{\text{IR}}^2]}{\sigma_{\text{IR}} \sqrt{2\beta_r \sigma_{\text{IR}}^2 + 2i}} \right) - 1 \right] + \frac{(-1)^{\frac{3}{4}} e^{-i\phi_{\text{CEO}}} e^{\frac{i\omega_{\text{IR}}^2 \sigma_{\text{IR}}^2}{2\beta_r \sigma_{\text{IR}}^2 - 2i}}}{\sqrt{2\beta_r \sigma_{\text{IR}}^2 - 2i}} \left[ \text{erf} \left( \frac{(-1)^{\frac{1}{4}} [(t-t_0)(\beta_r \sigma_{\text{IR}}^2 - i) + \omega_{\text{IR}} \sigma_{\text{IR}}^2]}{\sigma_{\text{IR}} \sqrt{2\beta_r \sigma_{\text{IR}}^2 - 2i}} \right) - 1 \right] \right\} \quad (\text{B.3})$$

where erf is the error function, and the second integral is:

$$\int_t^{+\infty} dt' \frac{A_{\text{IR}}^2(t')}{2} = \frac{A_0^2 \sqrt{\pi} \sigma_{\text{IR}}}{4} \left\{ \left[ 1 - \text{erf} \left( \frac{t-t_0}{\sigma_{\text{IR}}} \right) \right] + \frac{(-1)^{\frac{1}{4}} e^{2i\phi_{\text{CEO}}} e^{-\frac{i\omega_{\text{IR}}^2 \sigma_{\text{IR}}^2}{\beta_r \sigma_{\text{IR}}^2 + i}}}{2\sqrt{\beta_r \sigma_{\text{IR}}^2 + i}} \left[ \text{erf} \left( \frac{(-1)^{\frac{3}{4}} ((t-t_0)(\beta_r \sigma_{\text{IR}}^2 + i) + \omega_{\text{IR}} \sigma_{\text{IR}}^2)}{\sigma_{\text{IR}} \sqrt{\beta_r \sigma_{\text{IR}}^2 + i}} \right) - 1 \right] + \frac{(-1)^{\frac{3}{4}} e^{-2i\phi_{\text{CEO}}} e^{\frac{i\omega_{\text{IR}}^2 \sigma_{\text{IR}}^2}{\beta_r \sigma_{\text{IR}}^2 - i}}}{2\sqrt{\beta_r \sigma_{\text{IR}}^2 - i}} \left[ \text{erf} \left( \frac{(-1)^{\frac{1}{4}} ((t-t_0)(\beta_r \sigma_{\text{IR}}^2 - i) + \omega_{\text{IR}} \sigma_{\text{IR}}^2)}{\sigma_{\text{IR}} \sqrt{\beta_r \sigma_{\text{IR}}^2 - i}} \right) - 1 \right] \right\}. \quad (\text{B.4})$$

We exploited these expressions for computing the Volkov phase difference when multiple XUV pulses are present.

## Appendix C. Analytical solution for satellite XUV pulses

Starting from equation (2), where we define  $K = p^2/2$  as the final kinetic energy of the photoelectrons, we assume that the XUV pulse is much shorter than the IR one. In this condition, each XUV pulse generates a photoelectron wavepacket almost instantaneously, and their interaction with the IR field for  $t < \tau$  can be neglected. We can thus replace the Volkov phase defined in equation (3), which depends on  $t$ , with its value for  $t = \tau$ . Therefore, if  $\phi(t) \simeq \phi(\tau)$ , we obtain:

$$S(p, \tau) \simeq \left| e^{i\phi(\tau)} \int_{-\infty}^{+\infty} dt E_X(t-\tau) d[p] e^{i(K+I_p)t} \right|^2. \quad (\text{C.1})$$

Defining the streaked photoelectron wavepacket in the time domain as in equation (11), the squared modulus of its Fourier transform will give the spectrogram (equation (13)).



In typical experimental conditions, generating a perfectly isolated single attosecond pulse is challenging. Smaller pulse satellites separated by a half- or full-cycle of the driving radiation are often unavoidable, complicating the temporal structure of the XUV radiation. Here we assume the presence of one main XUV pulse and of a satellite pulse, either anticipated or delayed with respect to the main one. Since both pulses lead to the emission of a photoelectron wavepacket, we can describe their structure in the time domain as in equation (21), where  $\rho_r$  the amplitude ratio between the main pulse and its satellite and  $\delta_t$  is their distance in time. The phase term in equation (21) accounts for the delay-dependent sign of the pulse replica in the HHG process. For  $\delta_t = \pm\pi/\omega_{\text{IR}}$ , the sign of the driving field will be opposite in the emission of the two pulses, while for  $\delta_t = \pm 2\pi/\omega_{\text{IR}}$  the driving field will have the same direction in both emission events.

Under the previously discussed approximation, we can write the spectrogram as the squared modulus of the Fourier transform of the time-dependent photoelectron wavepacket in equation (21), and by exploiting the linearity of the Fourier transform we obtain:

$$S(p, \tau) = \left| e^{i\phi(\tau)} \mathcal{F}\{\chi_s(t, \tau)\} + e^{i\phi(\tau+\delta_t)} \rho_r e^{-i\omega_{\text{IR}}\delta_t} \mathcal{F}\{\chi_s(t - \delta_t, \tau - \delta_t)\} \right|^2 \quad (\text{C.2})$$

where  $\chi_s(t, \tau)$  is defined as in equation (11). From the time-shifting property of the Fourier transform (equation (7)), considering that  $\omega = p^2/2 + I_p$ , we can write:

$$S(p, \tau) = \left| e^{i\phi(\tau)} \mathcal{F}\{\chi_s(t, \tau)\} + e^{i\phi(\tau+\delta_t)} \rho_r e^{-i\omega_{\text{IR}}\delta_t} e^{-i(p^2/2+I_p)\delta_t} \mathcal{F}\{\chi_s(t, \tau - \delta_t)\} \right|^2. \quad (\text{C.3})$$

Collecting an  $e^{i\phi(\tau)}$  factor, associated with the Volkov phase of the main pulse, from both terms, we can then write:

$$S(p, \tau) = \left| \tilde{\chi}_s(p, \tau) + \rho_r e^{i\Delta\phi(\tau, \delta_t)} e^{-i\omega_{\text{IR}}\delta_t} e^{-i(p^2/2+I_p)\delta_t} \tilde{\chi}_s(p, \tau - \delta_t) \right|^2 \quad (\text{C.4})$$

where, being a pure phase term, we omitted the collected factor, and we defined the Fourier transform of the streaked photoelectron wavepacket  $\tilde{\chi}_s(p, \tau) = \mathcal{F}\{\chi_s(t, \tau)\}$ . In this expression, we defined:

$$\Delta\phi(\tau, \delta_t) = \phi(\tau - \delta_t) - \phi(\tau) \quad (\text{C.5})$$

as the difference of the Volkov phases for the satellite and the main pulse.

To calculate this quantity, we need to compute twice the analytical expression for the Volkov phase in the central momentum approximation derived in B. However, albeit analytical, this involves several evaluations of the error function, thus making the nonlinear fit computationally expensive. For many applications, an approximate evaluation [27] is enough. Assuming the integral of  $A_{\text{IR}}^2(t)$  negligible, if the central momentum is the same for all electron wavepackets, the difference in Volkov phase between the main pulse and the satellite can be written as:

$$\Delta\phi(\tau, \delta_t) \simeq p_c \cdot [B(\tau + \delta_t) - B(\tau)], \quad \frac{dB(t)}{dt} = A_{\text{IR}}(t). \quad (\text{C.6})$$

This expression can be evaluated much faster and gives accurate results when the IR amplitude is small enough.

In conclusion, by inserting into equation (C.4) the analytical expression of the IR field and the definition of photoelectron wavepacket in the frequency domain (equation (14)), we are able to fit the simulated and experimental spectrograms. Its generalization for a larger number of satellite pulses is straightforward.

## ORCID iDs

G Inzani  <https://orcid.org/0000-0002-0864-5976>  
 N Di Palo  <https://orcid.org/0000-0001-8386-6990>  
 G L Dolso  <https://orcid.org/0000-0002-7441-2660>  
 M Nisoli  <https://orcid.org/0000-0003-2309-732X>  
 M Lucchini  <https://orcid.org/0000-0001-6476-100X>

## References

- [1] Borrego-Varillas R, Lucchini M and Nisoli M 2022 *Rep. Prog. Phys.* **85** 066401
- [2] Geneaux R, Marroux H J B, Guggenmos A, Neumark D M and Leone S R 2019 *Phil. Trans. R. Soc. A* **377** 20170463
- [3] Goulielmakis E et al 2004 *Science* **305** 1267–9

- [4] Lucchini M, Castiglioni L, Kasmi L, Kliuiev P, Ludwig A, Greif M, Osterwalder J, Hengsberger M, Gallmann L and Keller U 2015 *Phys. Rev. Lett.* **115** 137401
- [5] Ossiander M et al 2018 *Nature* **561** 374–7
- [6] Inzani G et al 2023 *Nat. Photon.* **17** 1059–65
- [7] Locher R, Castiglioni L, Lucchini M, Greif M, Gallmann L, Osterwalder J, Hengsberger M and Keller U 2015 *Optica* **2** 405
- [8] Kasmi L, Lucchini M, Castiglioni L, Kliuiev P, Osterwalder J, Hengsberger M, Gallmann L, Krüger P and Keller U 2017 *Optica* **4** 1492
- [9] Lucchini M et al 2021 *Nat. Commun.* **12** 1021
- [10] Orfanos I, Makos I, Lontos I, Skantzakis E, Förg B, Charalambidis D and Tzallas P 2019 *APL Photonics* **4** 080901
- [11] Lucchini M, Sato S A, Schlaepfer F, Yabana K, Gallmann L, Rubio A and Keller U 2020 *J. Phys. Photon.* **2** 025001
- [12] Borsch M, Meierhofer M, Huber R and Kira M 2023 *Nat. Rev. Mater.* **8** 668–87
- [13] Zong A, Nebgen B R, Lin S-C, Spies J A and Zuerch M 2023 *Nat. Rev. Mater.* **8** 224–40
- [14] Amini K et al 2019 *Rep. Prog. Phys.* **82** 116001
- [15] Brabec T and Krausz F 2000 *Rev. Mod. Phys.* **72** 545–91
- [16] Itatani J, Quéré F, Yudin G L, Ivanov M Y, Krausz F and Corkum P B 2002 *Phys. Rev. Lett.* **88** 173903
- [17] Mairesse Y and Quéré F 2005 *Phys. Rev. A* **71** 011401
- [18] Trebino R, DeLong K W, Fittinghoff D N, Sweetser J N, Krumbügel M A, Richman B A and Kane D J 1997 *Rev. Sci. Instrum.* **68** 3277–95
- [19] Keathley P D, Bhardwaj S, Moses J, Laurent G and Kärtner F X 2016 *New J. Phys.* **18** 073009
- [20] Kane D 1999 *IEEE J. Quantum Electron.* **35** 421–31
- [21] Gagnon J, Goulielmakis E and Yakovlev V 2008 *Appl. Phys. B* **92** 25–32
- [22] Lucchini M, Brüggmann M, Ludwig A, Gallmann L, Keller U and Feurer T 2015 *Opt. Express* **23** 29502
- [23] Yu W-W, Zhao X, Wei H, Wang S-J and Lin C D 2019 *Phys. Rev. A* **99** 033403
- [24] Zhu Z, White J, Chang Z and Pang S 2020 *Sci. Rep.* **10** 5782
- [25] Dolso G L, Inzani G, Di Palo N, Moio B, Medeghini F, Borrego-Varillas R, Nisoli M and Lucchini M 2023 *APL Photonics* **8** 076101
- [26] Zhao X, Wang S-J, Yu W-W, Wei H, Wei C, Wang B, Chen J and Lin C D 2020 *Phys. Rev. Appl.* **13** 034043
- [27] Gagnon J and Yakovlev V S 2009 *Opt. Express* **17** 17678
- [28] Vismarra F, Borrego-Varillas R, Wu Y, Mocci D, Nisoli M and Lucchini M 2022 *J. Phys. Photon.* **4** 034006
- [29] Lucarelli G D, Moio B, Inzani G, Fabris N, Moscardi L, Frassetto F, Poletto L, Nisoli M and Lucchini M 2020 *Rev. Sci. Instrum.* **91** 053002
- [30] Cavalieri A L et al 2007 *Nature* **449** 1029–32
- [31] Neppel S, Ernstorfer R, Bothschafter E M, Cavalieri A L, Menzel D, Barth J V, Krausz F, Kienberger R and Feulner P 2012 *Phys. Rev. Lett.* **109** 087401
- [32] Schlaepfer F, Lucchini M, Sato S A, Volkov M, Kasmi L, Hartmann N, Rubio A, Gallmann L and Keller U 2018 *Nat. Phys.* **14** 560–4
- [33] Khan S U, Xie M-F, Zhong M-C, Wang S, Yan P-G and Jiang W-C 2023 *New J. Phys.* **25** 083014
- [34] Gagnon J and Yakovlev V S 2011 *Appl. Phys. B* **103** 303–9
- [35] Wang H, Chini M, Khan S D, Chen S, Gilbertson S, Feng X, Mashiko H and Chang Z 2009 *J. Phys. B: At. Mol. Opt. Phys.* **42** 134007
- [36] Yakovlev V S, Gagnon J, Karpowicz N and Krausz F 2010 *Phys. Rev. Lett.* **105** 073001
- [37] Zhao X, Wei H, Wei C and Lin C D 2017 *J. Opt.* **19** 114009
- [38] Pedrelli L, Keathley P D, Cattaneo L, Kärtner F X and Keller U 2020 *New J. Phys.* **22** 053028
- [39] Marr G and West J 1976 *At. Data Nucl. Data Tables* **18** 497–508
- [40] Mauritsson J, Gaarde M B and Schafer K J 2005 *Phys. Rev. A* **72** 013401
- [41] Schultze M et al 2013 *Nature* **493** 75–78
- [42] Schultze M et al 2014 *Science* **346** 1348–52
- [43] Siegrist F et al 2019 *Nature* **571** 240–4
- [44] Goulielmakis E et al 2008 *Science* **320** 1614–7
- [45] Chini M, Zhao K and Chang Z 2014 *Nat. Photon.* **8** 178–86
- [46] Mashiko H, Gilbertson S, Li C, Khan S D, Shakya M M, Moon E and Chang Z 2008 *Phys. Rev. Lett.* **100** 103906
- [47] Chini M, Wang H, Khan S D, Chen S and Chang Z 2009 *Appl. Phys. Lett.* **94** 92–95